

## Increasing scanning speed during induction thermography tests: simulations and experimental tests to investigate crack detectability.

by E. D'Accardi\*, G. Dell'Avvocato\*\*, I.O. Del Rosso\*, G. Di Franco\*, U. Galietti\*, D. Palumbo\*

\* Polytechnic of Bari, Department of Mechanics, Mathematics and Management (DMMM), Via Edoardo Orabona - 70125 Bari, Italy, [ester.daccardi@poliba.it](mailto:ester.daccardi@poliba.it), [i.delrosso1@studenti.poliba.it](mailto:i.delrosso1@studenti.poliba.it), [g.difranco@studenti.poliba.it](mailto:g.difranco@studenti.poliba.it), [umberto.galietti@poliba.it](mailto:umberto.galietti@poliba.it), [davide.palumbo@poliba.it](mailto:davide.palumbo@poliba.it)

\*\* University of L'Aquila, Industrial and Information Engineering and Economics, Piazzale Ernesto Pontieri 1, Monteluco di Roio - 67100 L'Aquila, Italy, [giuseppe.dellavvocato@univaq.it](mailto:giuseppe.dellavvocato@univaq.it)

### Abstract

Induction thermography has emerged as a robust non-destructive testing (NDT) method for detecting surface cracks in various materials. This study investigates the capability of induction thermography in surface crack detection by analysing Probability of Detection (POD) curves and employing a Finite Element Model (FEM) to explore the influence of high scanning speed on crack detection.

The research is divided into two main parts: experimental tests and simulations. In the experimental phase, induction thermography was applied to detect surface cracks in metallic specimens. The raw thermal data, acquired at a consistent scan speed ( $\approx 11$  km/h), were processed to reconstruct the sequences and identify cracks. The results, expressed as thermal contrast at the crack tips, were used to construct POD curves, which provide a statistical representation of the detection capability of the method, correlating the probability of detecting a crack with changes in defect depth.

In the simulation phase, a preliminary FEM was developed to replicate the induction thermography process. The model simulates the thermal response of the specimen with surface cracks under different scanning speeds of the induction coil, extrapolating the thermal behaviour at higher scan speeds. The influence of speed on the contrast was examined to explore the possibility of increasing this parameter for railway applications.

Keywords: crack detection; induction thermography; non-destructive technique (NDT); FEM model; POD curves.

### 1. Introduction

Non-destructive testing (NDT) methods are crucial for ensuring the integrity and safety of structural components in various industrial fields, including aerospace, automotive, and civil engineering. Surface cracks, particularly in critical infrastructure such as railway tracks, pose significant safety hazards. Railway tracks are subjected to dynamic loads and harsh environmental conditions, which can lead to the initiation and propagation of cracks. Early detection of these defects is crucial to prevent catastrophic failures and ensure the safety and reliability of railway operations [1]-[3].

Non-destructive testing (NDT) for rail defect detection involves methods like ultrasonic testing, eddy current testing, and thermography to identify flaws and identify typical defects. Thermography offers advantages due to its ability to quickly detect surface and subsurface defects by visualizing temperature variations, allowing for a full field and comprehensive inspections [2]-[10].

Among the various NDT techniques, induction thermography has garnered significant attention for its ability to detect and characterize surface cracks in conductive materials. This method involves inducing eddy currents in the material using an electromagnetic coil, with a different thermal behaviour and distribution of currents around the defective area, subsequently revealed by infrared thermography with a higher thermal contrast [4]-[7].

Induction thermography offers several advantages, such as rapid inspection times and covering large areas without a direct contact with the material. For these reasons, and above all, for the possibility to detect short cracks, this technique represents a promising solution for regular and efficient inspection of railway tracks [8]-[11].

However, the performance of this method can be influenced by various factors, including the scanning speed of the induction coil, which affects the thermal contrast and resolution of detected cracks. Understanding the impact of scanning speed on the detection capabilities of this technique is essential for optimizing inspection tests and procedures for data analysis.

Probability of Detection (POD) curves are widely used in NDT to quantify the reliability and effectiveness of a detection method. These curves represent the likelihood of detecting a defect as a function of defect sizes and depths and are crucial for assessing the performance of NDT techniques [12]-[15]. In parallel, Finite Element Modelling (FEM) serves as a powerful tool for simulating the induction thermography tests, enabling the analysis and evaluation of various parameters, including scanning speed, without the need of extensive experimental campaigns [6], [16]-[19]. Although different works in literature investigated induction thermography and crack detection, even obtaining the Probability of Detection (POD) curves with simulated and experimental results [6], these studies are limited to static tests, employing post-processing algorithms for data analysis not sustainable and available at high speeds [10]; for these reasons, the

influence of scan speed on detection limits and correlation of this parameter with geometrical characteristics of the crack is still an open point.

This study aims to integrate experimental induction thermography with FEM simulations to investigate the influence of very high scanning speeds on the detection of surface cracks. After generating POD curves from experimental data at different scan speeds ( $\approx 11$  km/h) based on the analysis of the thermal contrast at the crack tips after a first post processing of the data, the experimental results have been validated with a preliminary FEM model developed in COMSOL Multiphysics® v 5.6, for extrapolating the results at higher speed.

## 2. Material and methods

### Experimental setup and tests

Experimental tests have been carried out using the setup shown in Figure 1a, with the indication of the main devices. A FLIR LWIR cooled camera was adopted, considering a frame rate of 1800 Hz and a spatial resolution of 0.25 mm/pixel. A commercial inductor up to a power of 4.2 kW has been used, designing a coil of solenoid circular shape with the geometrical parameters and technical specification resumed in Table 1. A S355J2 specimen with the geometry reported in Figure 1b was considered for the investigation. The image shows that the specimen presents several open cracks produced by electrical discharge machining (EDM) process with different 12 depths, simulating known thickness open crack of about 0.4 mm and length of 10 mm (DIN 54193:2018-02) [20]-[26]. A black coating has been used to cover the specimen increasing its emissivity (about 0.95) and making it uniform in value. The validation involved several static tests by changing the pulse duration, reaching a power of 2.7 kW (240 A), while for the dynamic case, the plate speed was changed three times, reaching about 3.5, 6.6 and 11 km/h. Each test was repeated five times, to design POD curves and validate the FEM model with a good degree of confidence, considering cracks at different depths and at the adopted three speeds. A resume of testing parameters for excitation and acquisition is reported in Table 2.

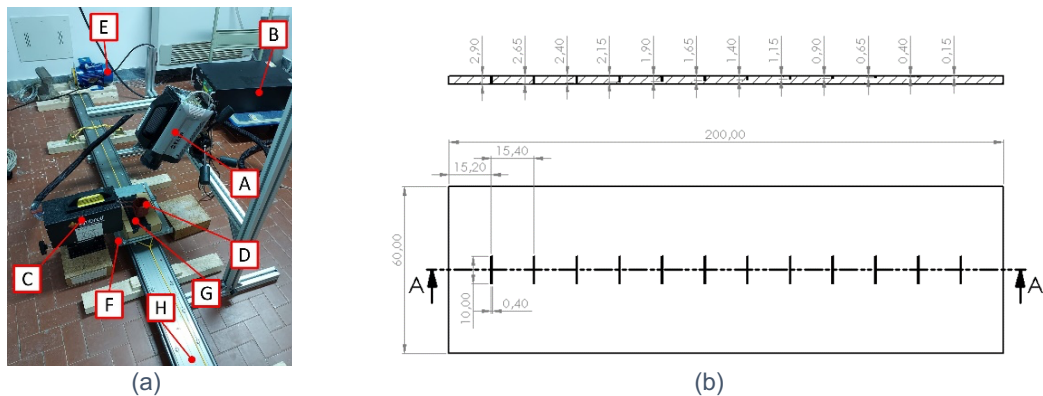


Figure 1. (a) Set-up adopted for induction tests: A – FLIR cooled camera, B – inductor generator, C – inductor head, D – coil, E – towing motor, F – piece holder table, G – specimen, H – towing guide and (b) schematic representation of the tested specimen, with 12 cracks of depths 0.15 – 2.90 mm (step 0.25 mm), length 10 mm, and opening 0.4 mm.

Coil Diameter (mm)	Coil Height (mm)	Turns number	Inductance ( $\mu$ H)	Excitation frequency (kHz)
60	50	9	3.23	177

Table 1. Coil geometrical parameters and technical specifications.

Induced Current (A)	Power (kW)	Distance from the specimen surface (mm)	Frame rate (Hz)	Geometrical resolution (mm/pixel)	Scan speed (km/h)
240	2.7	10	1800	0.25	3.5, 6.6, 11

Table 2. Adopting testing parameters for the acquisition and the excitation.

### Procedure for data analysis

Considering the possible application of the technique at very high scan speeds, the analysis of the experimental results and later validation of the FEM model concerned the cooling phase and a portion of the entire frame shown in Figure 1b. In particular, in the case of a speed of 3.5 km/h, considering the adopting testing parameters and results in terms of temperature increase, the useful frames for further analyses and model validation are about 100, corresponding to a time window of 80 ms (Figure 2a, red lines).

A reconstruction algorithm has been developed to have the possibility of analysing the entire specimen with a single frame that represents a precise instant time after the coil excitation (Figure 2b, at a distance of about 20 mm from the coil, considering as reference the time in which the crack tip is under the coil respect to the crack position). This

reconstruction regards the analysis of a single profile in case of low speed, a matrix of few columns in case of high speeds, as already demonstrated in [10].

As the results in Figure 2b and 2e demonstrate, there is an influence of the non-uniform heating and coil reflections that cannot be compensated applying usual post-processing algorithms or simple cold frame subtraction as in case of static tests [10]. For these reasons, a median filter of kernel size 31x31 pixels (Figure 2c) has been applied to each single frame after the sequence reconstruction. This latter has been subtracted to the original reconstructed sequence to filter the non-homogeneous heating (Figure 2b – Figure 2c). The result shown in Figure 2d is, directly, a measure of the thermal contrast at a given time (or distance from the coil excitation). As the plot in Figure 2e demonstrates, thanks to the filter application, the non-uniformity of heating and the reflections are compensated, with a reduction in the resulting contrast.

To evaluate the probability of detection as function of crack geometrical characteristics, the maximum signal at the crack tip has been evaluated considering both the tips to consider the influence of coil distance. The POD curves are obtained following the standard ASTM E3023-15; for this purpose, a linear relationship between a continuous measure of the system response “ $\hat{a}$ ” (e.g. the contrast-to-noise ratio of a temperature difference in a thermogram (CNR<sub>T</sub>) obtained considering as measure of the noise the standard deviation related to a sound area highlighted in black in Figure 2d, and the contrast in correspondence of the crack tip, selecting the maximum value for each crack) and a parameter “ $a$ ” describing the defect needs to be detected. The parameter “ $a$ ” can be any mathematical representation of one or more physically reasonable parameters of crack detection like, in this case, the defect surface depth  $d$ . The coil distance is considered as noise source, assigning both values that identify the contrast at the crack tip at the same depth to find a unique POD curve. The choice related to the definition of a threshold value in a POD curve represents the specific point at which the likelihood of detecting a crack or, more in general, a defect meets or exceeds a predetermined probability, often used to determine the minimum detectable crack size or depth with a certain confidence level. As demonstrated in previous works, and after a preliminary evaluation with different threshold values, a threshold value of 2 balance sensitivity in defect detection. A threshold of 2 has been selected based on empirical data indicating that this value optimally distinguishes between true positives (actual defects) and false positives (non-defective cases).

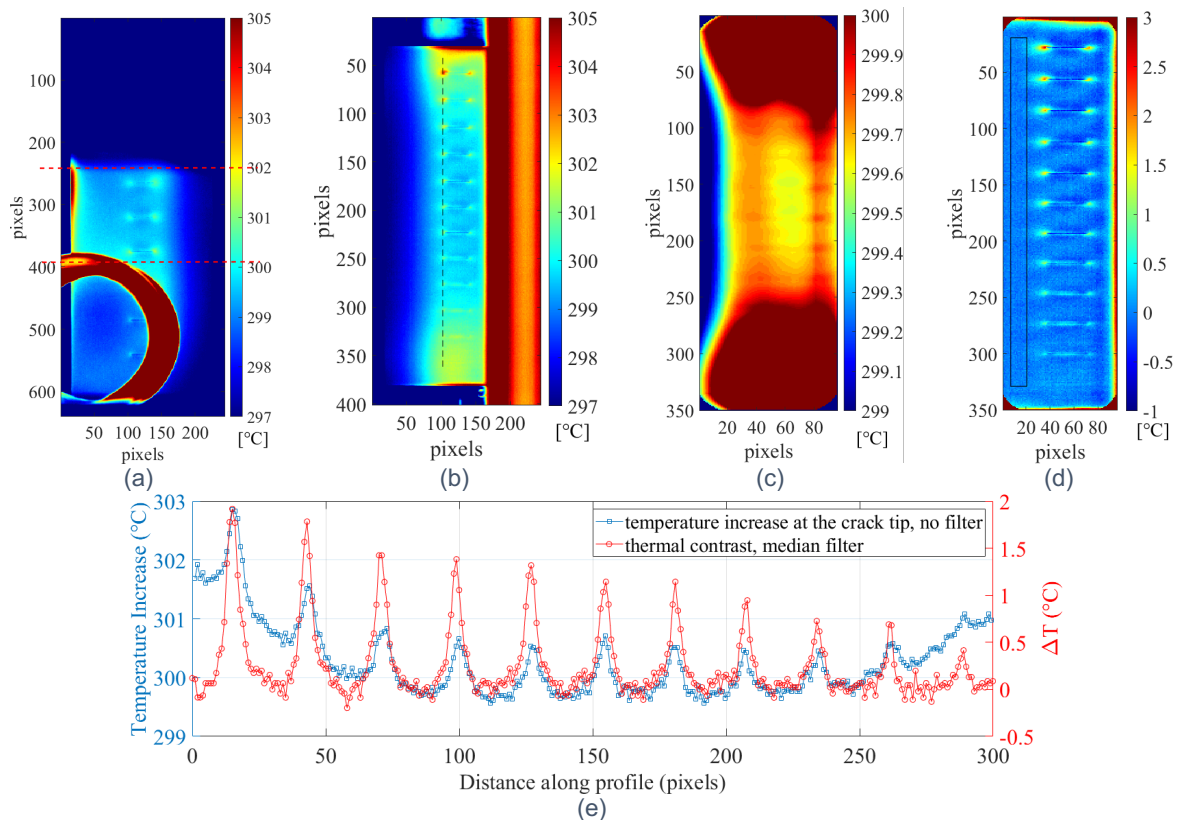


Figure 2. (a) A thermographic map to represent the portion of frame used for data analysis and validation, (b) frame after the coil excitation ( $\approx 20$  mm) after the reconstruction, (c) frame filtered with a median filter (kernel size 31x31 pixels), (d) frame obtained after a subtraction of the results in Figure 2b and 2c, (e) thermal behaviour in correspondence of the crack tip – dotted black line in Figure 2b before and after the filter application.

### FEM Model and validation

A 3D finite element model (FEM) was developed using COMSOL Multiphysics® considering a plate of the same size as the one investigated with experimental tests, of finite thickness, with a single crack, changing defect depth for each simulation to reproduce the geometry shown in Figure 1b.

The coil used in the model is geometrically reproduced as a hollow cylindrical body using the function homogenized multi-turn, defining the number of turns, diameter, and axial pitch as well as in the experimental case. The thermophysical properties of the plate material considered in the simulations refer to the material used in the railway industry, that is S355J2 steel, and are summarised in Table 3.

Thermal capacity $C_p$ [J/kgK]	Thermal conductivity $k$ [W/mK]	Density $\rho$ [kg/m <sup>3</sup> ]	Electrical conductivity $\sigma$ [S/m]	Relative permeability magnetic $\mu_r$
500	40	8000	$1.82 \times 10^6$	100

Table 3. Thermophysical and electrical properties adopted for FEM simulations.

Two models were created, first considering the static case, already widely discussed in the literature [6], and then moving on to the dynamic case (Figure 1b). In the case of induction simulations, considering the thermal diffusion length and eddy current penetration depth, it is essential to use the correct mesh to assess the eddy currents for each imposed crack depth. To do this, a composite six-node prismatic element, composed of six layers, each of thickness equal to  $\delta/2$ , with  $\delta$  representing the standard penetration depth (for this material, considering an excitation frequency of about 180 kHz and the material electrical properties this value is around 0.03 mm, so about 100 elements along the entire specimen thickness), was created. A mesh of 55576 elements has been adopted.

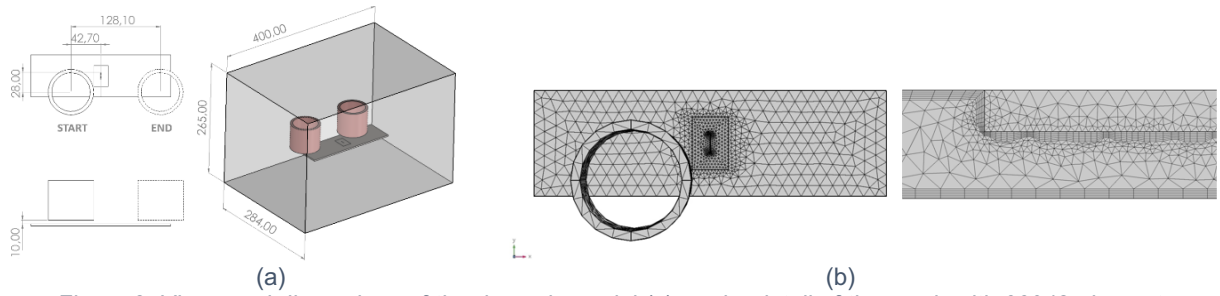


Figure 3. Views and dimensions of the dynamic model (a), and a detail of the mesh with 66048 elements, mesh with 128944 elements and a zoom of shell prismatic elements (b).

As already said, the validation concerns many cases, in terms of speed, defect depth and relative position between coil turns and crack tip. The FEM for induction thermography involves several key equations that describe the electromagnetic and thermal phenomena occurring during the inspection, included well-known Maxwell's equations for magnetic field and the modified heat transfer equation to consider the motion of the specimen surface respect to the induction source, here reported:

$$\rho c_p \left( \frac{\partial T}{\partial t} + v \cdot \nabla T \right) = \nabla \cdot (k \cdot \nabla T) + Q \quad (1)$$

where  $v$  represents the relative speed between specimen and induction coil,  $k$  is the thermal conductivity,  $T$  is the temperature  $Q$  is the internal heat generation per unit volume (due to eddy currents),  $\rho$  is the material density and  $c_p$  is the specific heat capacity. In addition, some boundary conditions in correspondence of the nodes must be defined, including the magnetic fields (Ampere law and magnetic insulation) and the impedance boundary condition. Impedance boundary condition is a node that describes the boundary condition useful when the electromagnetic field penetrates the domains for small distances of the selected surface. It is used to consider the skin effect due to induced currents when their penetration standard depth is much smaller than the thickness of the conductor. The additional equation that the interface solves is:

$$\sqrt{\frac{\mu_0 \mu_r}{\varepsilon_0 \varepsilon_r - \frac{j\sigma}{\omega}}} \bar{n} x \bar{H} + \bar{E} - (\bar{n} \cdot \bar{E}) \bar{n} = (\bar{n} \cdot \bar{E}_s) \bar{n} - \bar{E}_s \quad (2)$$

where  $\bar{E}$  is the electric field,  $\bar{E}_s$  is the surface electric field,  $H$  is the magnetic field intensity,  $\mu$  is the magnetic permeability,  $\varepsilon_r$  is the relative electric permittivity,  $\varepsilon_0$  is the vacuum electric permittivity and  $\sigma$  is the electrical conductivity. This equation represents an approximation of the penetration of electromagnetic fields into the domains of interest, reducing the computational effort. The node applies only to the external surfaces of the domains and requires, as initial values, the modules of the components of the surface electric field  $\bar{E}_s$ . In this case, this boundary condition was applied to all external surfaces of the plate domain also including the internal walls of the crack; the components of  $\bar{E}_s$  have been placed all equal to zero.

For model validation, experiments with different scan speeds were considered, identifying the area at the crack tips and the related sound. The simulated data have been extracted, defining these points as a geometrical data set, considering the adopted frame rate to export the data after simulations and the same geometrical resolution of the experiments (Figure 4). The same boxes were selected both for simulations and experiments, considering the maximum temperature value in correspondence of the crack tip, and the mean value in a ROI of 3x3 pixels was than considered to define the sound value, at an approximate distance of 8 mm. The part related to the temperature cooling after coil excitation, for the three different speeds has been considered for the validation, starting from the first frame available after coil excitation. This physical distance corresponds to different instants of time when the speed change. Depending on the

adopted scan speed, the number of data or frames available changes until to reach 25 data available in case of experiments at 11 km/h. The experimental data considered for the validation were not filtered as described before, to not further process the simulation results. The variability related to the relative position between coil and crack tip was also considered, validating the model in the two different positions (indicated with  $\alpha$  and  $\beta$  in Figure 4a); the validation also concerned different crack depths. The contrast between defect and sound was considered as a key parameter for the validation. Then, different scan speeds were considered as input data for the simulations, reaching 50 km/h, simulating as intermediate steps 20, 30, 40 km/h. To compare the obtained results and evaluating the agreement between simulations and experiments, indexes as RMSE, maximum deviation and residual plots were considered. Five replications were considered for each experiment, and the average profile was used as a reference for the validation.

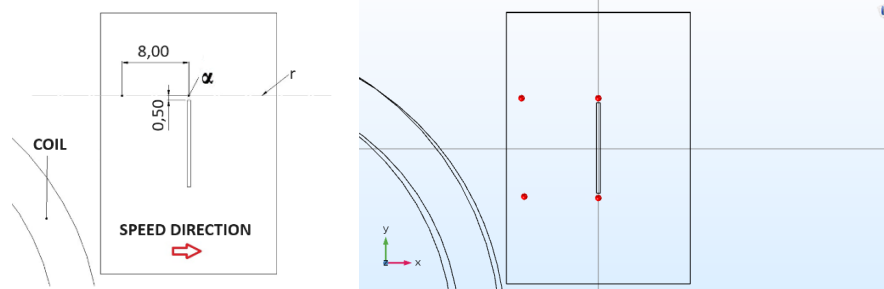


Figure 4. Scheme to representing the selected areas that identify crack tips and sound in the simulations.

### 3. Results and discussion

#### POD curves

The experimental data have been analysed as described in the previous section. For each value of the scan speed, a different POD curve has been obtained by analysing the data in terms of apparent temperature at the same physical distance from the coil. As anticipated, considering the different speeds of the specimen, but with the same profile to reconstruct the data, different time instants related to the cooling down phase have been selected. Considering a speed of 3.5 km/h the curve refers to about 23 ms as a time of cooling, 11 ms in case of 6.6 km/h, and 7 ms for 11 km/h. As the speed changes, also the heating time is different. Considering the coil diameter as an indication of this parameter, in correspondence of a speed of 3.5 km/h the excitation time is about 65 ms, 35 ms for 6.6 km/h, and 21 ms for 11 km/h. Giving constant the power and the current, also the energy density, defined as the integral of the power over the heating time, changes with speed. Based on the adopted frame rate, the precise position of the profile after the coil excitation can be available or not, as explained before in [10]. For these reasons, when the speed increases, it is recommended to reconstruct the sequence with a matrix instead of a profile, in order to not lose millimeters and so possible defects during the scanning [10].

Figure 5 presents the results obtained at a speed of 3.5 km/h, showing the contrast and then the normalized contrast as a function of the crack depth. The data corresponding to all the crack tips have been merged, irrespective of their position relative to the coil, treating these measurements as replications of the same test. The same Figure 5 also presents the results after binarization, using a threshold value of 2 and considering one replication as an example. For the last defect, with a shallow depth of 0.15 mm, white pixels appear at the crack tip when the threshold is set to 2, indicating the presence of a defect.

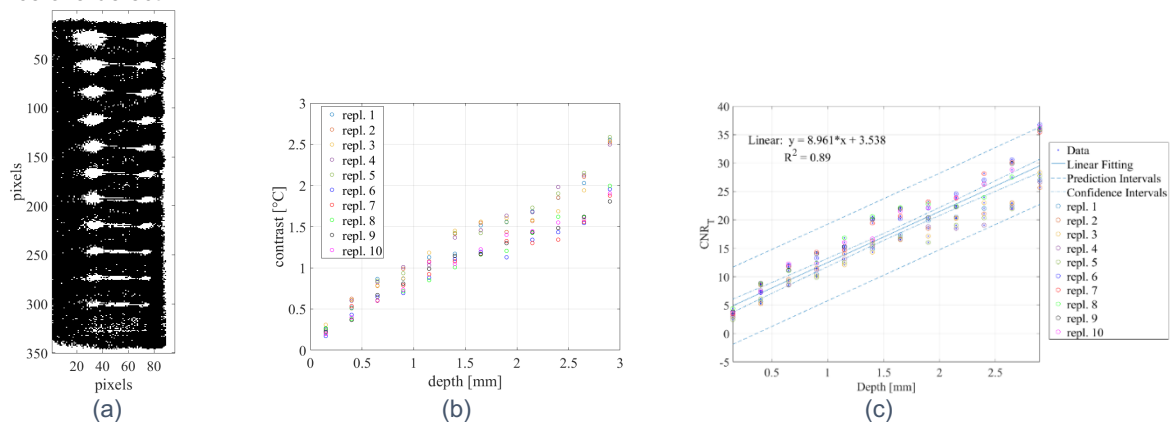


Figure 5. (a) Experimental results with a speed of 3.5 km/h – linear correlation between depth and normalized contrast and (b) binarized result with a threshold value equal to 2.

According to the standard, the POD curves were then obtained, repeating the same procedure also for the other tests at a different scan speed. Figure 6a shows the result at different speeds in terms of  $CNR_T$ , considering for simplicity

of representation the lower and higher speed (3.5 and 11 km/h), instead Figure 6b reports the POD curves, for the three different speed values. In particular, Figure 6a shows the linear relationship linking depth and  $CNR_T$ , and the 95% confidence bands relating to the adopted model. Considering that these data are related to the thermal contrast (not processed signal) and taking into account the noise generated by the variability due to the relative position between the coil tip and the crack, the obtained correlation can be considered good.

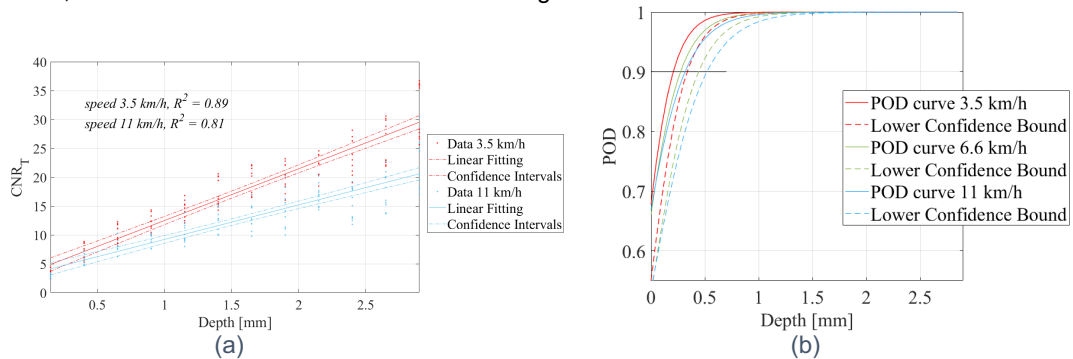


Figure 6. Comparing the results at different scan speeds in terms of (a)  $CNR_T$  and (b) POD curves.

Figure 6b also displays the confidence bands and the 90% reference line. The intersections of these lines with the main curve define the probability of identifying a defect with 90% probability and 95% confidence, in the case of the dashed curve, respectively. Table 4 reports this result as final summary indicating the depth values in correspondence of these points for the three different scan speeds.

Speed 3.5 km/h		Speed 6.6 km/h		Speed 11 km/h	
$a_{90}$	$a_{90/95}$	$a_{90}$	$a_{90/95}$	$a_{90}$	$a_{90/95}$
0.20	0.35	0.25	0.45	0.30	0.55

Table 4. A summary of the POD results for the different scan speeds.

Although this result is influenced by the statistical basis of the POD curve and in particular the definition of a linear model, key variables, and a threshold value, the probability at 90% and the overall POD decrease as speed increases, with the depth range reducing by approximately 0.05 mm (0.10 mm as confidence value  $a_{90/95}$ ).

For completeness, Figure 7 presents an example of the obtained results as maps showing the thermal contrast at speeds of 6.6 (Figure 7a) and 11 km/h (Figure 7b), considering the data related to any replication and applying the filtering and reconstruction procedure previously explained. In particular, for a speed of 6.6 km/h, a ROI of 4 pixels has been adopted for the reconstruction, instead 7 pixels have been considered for the tests at 11 km/h.

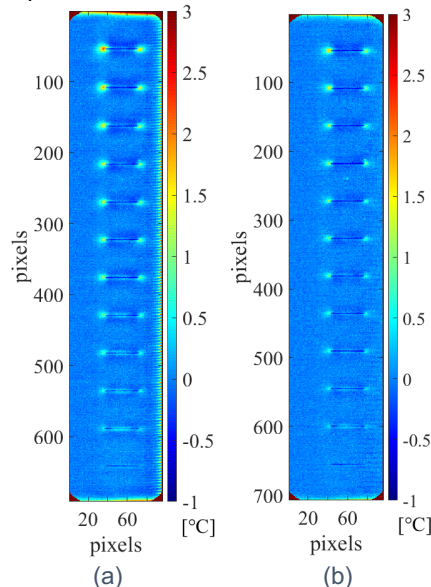


Figure 7. Results related to the thermal contrast after reconstruction and filtering operations at speeds of (a) 6.6 km/h and (b) 11 km/h.

**FEM validation and results at high scan speeds**

Figure 8a shows an example of the obtained results in terms of thermal contrast, comparing simulations and experimental data in the case of a crack depth of 2.65 mm, considering the tip indicated with  $\alpha$ , that is the closest to the coil turns. Experimental results are in good agreement with the numerical ones, although the complexity in determining the relative position between crack and coil and the exact frame available in the experiments after the coil passing. Considering the procedure for data analysis explained before, both for simulations and experiments, it was possible to obtain the results shown in Figure 8a. These results represent for the experiments the five different replications and the average profile, instead for the simulations a single profile with a double line. As highlighted before, the indication of the residual plot is also reported, with reference to the average profile for the experimental data. The validation regards the cooling phase, for this reason Figure 8b reports a zoom of the cooling phase based on the frames available in the experiments due to the frame window adopted to observe the specimen in motion. There is a good agreement between simulations and experiments, with a random distribution of the residuals (no particular trend is observed) and values of RMSE equal to 0.1044, and maximum deviation of 0.2412 between the average experimental profile and the simulation.

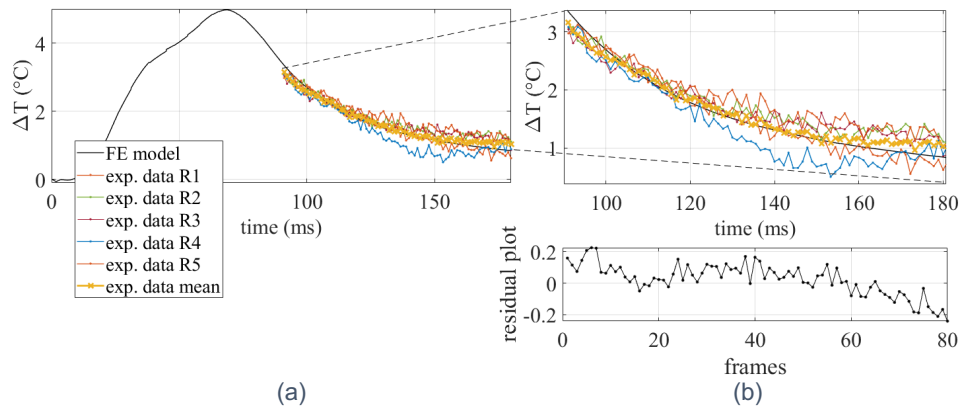


Figure 8. (a) Simulation and validation considering a crack of 2.65 mm depth, position  $\alpha$ , and the plate moving at a speed of 3.5 km/h, (b) with a zoom for the cooling down and the related residual plot to compare simulation and experimental data.

The results in Figure 9a and 9b are instead related to the validations at 6.6 km/h and 11 km/h considering the same approach explained before. Even in these cases the results are in good agreement, with values of RMSE and maximum deviation very low (6.6 km/h – RMSE 0.3367, MD 0.4892, 11 km/h – RMSE 0.9658, MD 1.1324).

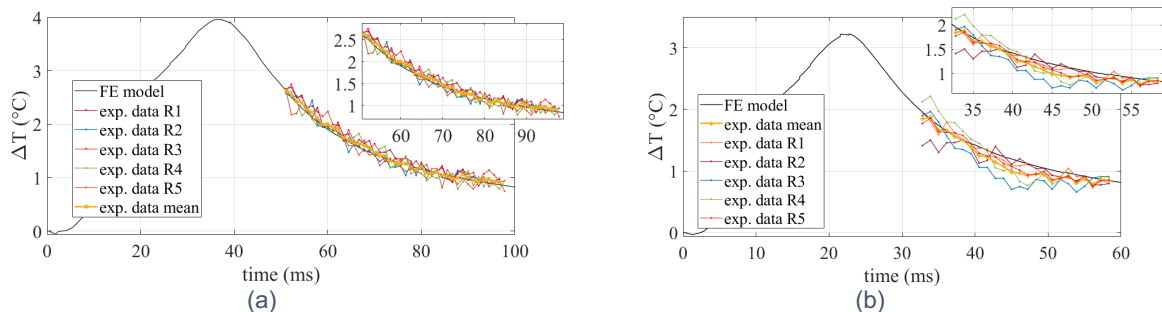


Figure 9. Simulation and validation considering a crack of 2.65 mm depth and the plate moving at a speed of (a) 6.6 km/h, and (b) at a speed of 11 km/h.

Considering the possibility of extracting the thermal behaviour at higher scan speeds from the numerical study after the validation at three different scan speeds and for different crack depths and positions between coil and crack, some simulations have been carried out up to 50 km/h. Figure 10 reports a graph that summarizes the obtained results in this sense, for 4 different levels of scan speeds, considering the crack with the same depth showed before (2.65 mm) and the same crack tip position.

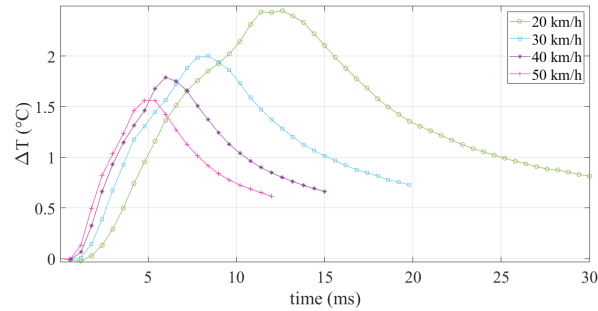


Figure 10. Simulation results considering different speeds for the crack with a depth of 2.65 mm and the position between coil and tip indicated with  $\alpha$ .

As explained before, based on the frames available to acquire the data and the investigated levels of speeds, the excitation time changes, together with the milliseconds available for the analysis during the cooling down. However, other factors, such as the adopted frame rate, must be considered for interpreting the results.

If the position of the extracted profile is always the same (about 20 mm from the coil) with a different indication of time in milliseconds after the coil excitation. In that case, it is theoretically possible to obtain the result in Figure 11 that demonstrates an exponential decrease in thermal contrast with the scan speed. However, for a crack depth of 2.65 mm, a contrast of about 1.5 °C can be still observed, with a concrete possibility to detect a significant signal at crack tip at a very high scan speed. Although the simulated data were subsampled at the same frequency used in the experimental tests, the obtained value remains theoretical.

A similar correlation and indication of the contrast as function of the scan speed can be obtained if a precise time after the coil excitation is instead analysed. However, the obtained results demonstrate that is primary to select the first data available after the coil excitation to have a good contrast even if at higher speeds.

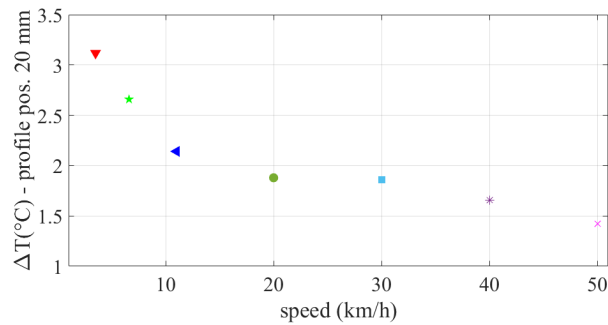


Figure 11. Simulation results considering different speeds for the crack with a depth of 2.65 mm and the position between coil and tip indicated with  $\alpha$  – position 20 mm after coil excitation.

For completeness, it is necessary to highlight that the theoretical end of excitation does not coincide with the maximum contrast which occurs shortly before the end of the coil passage, as shown in Figure 12 (speed of 50 km/h). These two maps are related to the apparent temperature and correspond to the position where the maximum contrast value occurs and the specific time during the cooling period, approximately 20 mm after the coil passes. The maximum contrast occurs at a given time depending on the relative positions of the coil and the crack tip in the 2D plane. The colormap adopted for the coil representation is referred to the magnetic flux density (mf). The obtained results reveal, as highlighted before, the possibility to detect a surface crack with these geometrical characteristics even if at a speed of 50 km/h.

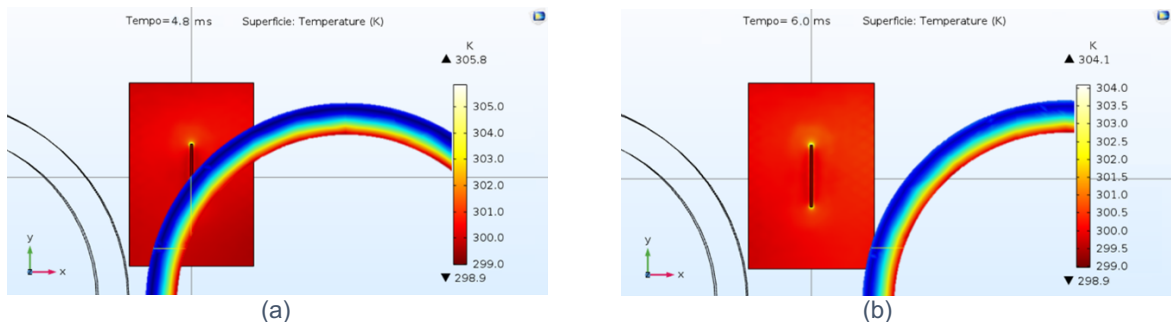


Figure 12. Simulation results considering a speed of 50 km/h for the crack with a depth of 2.65 mm and the position between coil and tip indicated with  $\alpha$  that maximizes the thermal contrast (a), together with the position during the cooling down chosen for the analysis (b).

Figure 13 presents the simulation results alongside various crack depths at speeds of 3.5 km/h and 50 km/h. The depicted values correspond to five different depths—specifically, 0.65, 1.15, 1.65, 2.15, and 2.65 mm—marked to highlight the positions analysed during the experiments. As demonstrated by the experimental results at lower speeds, contrast varies with crack depth, with a decrease in slope of approximately 40% as speed increases. Comparing the experimental results depicted in Figure 1b with the simulation results summarized in red in Figure 13c, there is a difference of about 1°C. This difference can be attributed to the presence of noise and median filter operations applied during the analysis of experimental data. At the shallowest depth for a speed of 50 km/h, the contrast was found to be very low, difficult to detect with experiments due to additional factors such as frame rate limitations and noise, which contribute to contrast reduction. Considering the disparity between experimental and simulation results, it can be concluded that a contrast of approximately 1.5 - 2 °C in simulations may be deemed adequate for providing an indication at the crack tip.

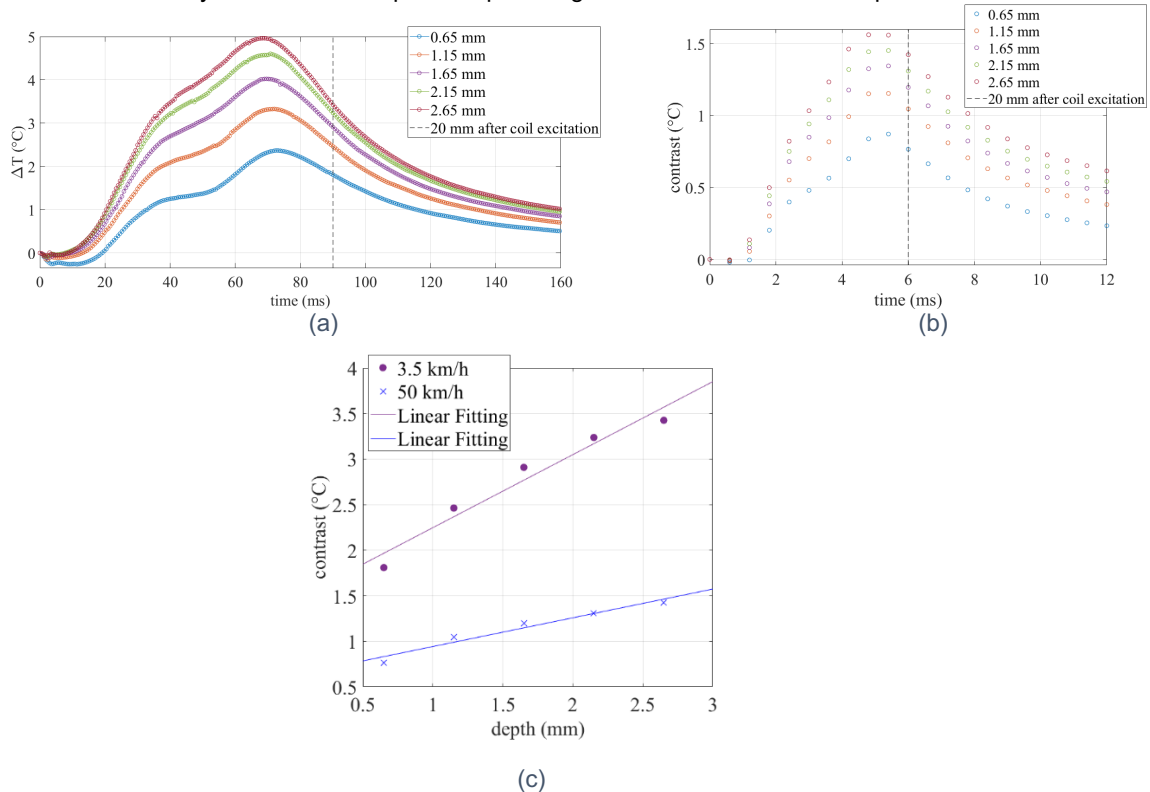


Figure 13. Simulation results – (a) thermal contrast for different crack depths at a speed of 3.5 km/h, (b) thermal contrast for different crack depths at a speed of 11 km/h and (c) theoretical correlation between crack depth when the data at 20 mm after the coil excitation are analysed.

The influence of the reciprocal position between coil and crack is instead reported in Figure 14, for the three different speed values, considering a crack depth of 2.65 mm. The results demonstrate that, independently from the scan speed, if the cooling is considered for data analysis, there is a reduction of the contrast of about 50% when the position between the crack tip and coil changes, considering, as in the experimental tests, a crack length of 10 mm.

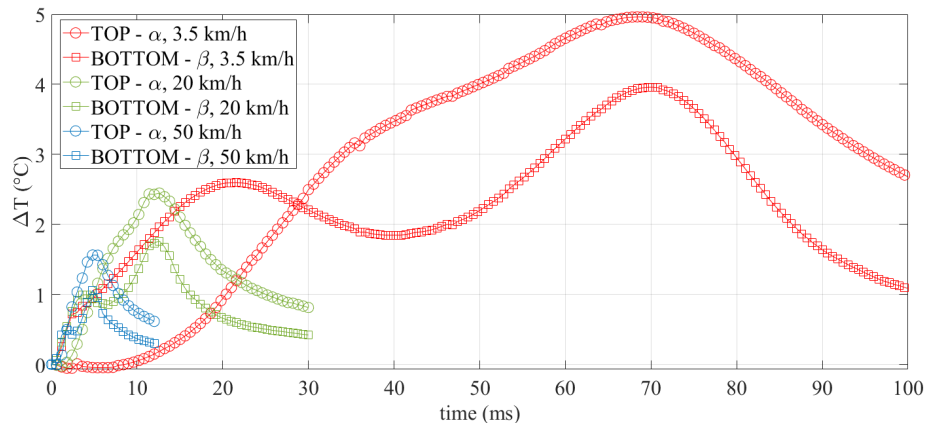


Figure 14. Simulation results at different speeds to represent the influence of the reciprocal position between crack tip and coil turns.

#### 4. Conclusions

This research aims to comprehensively understand how scanning speed affects the thermal response and detection limits in induction thermography. Experimental tests and simulations have been conducted to offer quantitative insights for applications requiring speeds of 20-50 km/h, with the primary goal of detecting surface cracks. Experimental Probability of Detection (POD) curves were derived by analysing thermal data from tests carried out at speeds between 3.5 and 11 km/h. These tests demonstrated the capability to detect surface cracks with very shallow depths of approximately 0.3 - 0.5 mm. A numerical model, validated for three different speeds with very good results, was subsequently used to extrapolate information for much higher speeds, indicating the feasibility of using this technique at speeds not previously investigated. Although these results are based on a numerical model and obtained through an extrapolation of thermal behaviour, the observed contrasts are sufficient to provide indications at deeper crack tips comparable to those detected at lower speeds in correspondence of shallow depths during experimental tests. Experimental results and simulations provide also quantitative indications about the influence of the crack depths and the coil position respect to the crack tip, demonstrating once again the strong dependence of the results obtainable from the use of this technique when these geometric and setup parameters change. Practical indications about the use of this technique have been also provided, as the possibility to adopt a median filter instead complex algorithms for data analysis in order to avoid effects due to a non-uniform heating, very common in case of the application of induction thermography, and once again the possibility of using the thermal contrast for speed tests where data processing is not possible. Future works will also provide indications considering different crack lengths, and the obtained results will be merged to obtain POD curves as functions of crack depth and length together. Furthermore, the influence of other parameters, as the surface with a different emissivity will be investigated in detail.

#### Acknowledgements

The authors wish to thank Tesmec Rail and, in particular, Ing. Gianluca Fumarola and Ing. Gaetano Marinelli for providing the master specimen used in this research.

#### Funding

Part of the work has been Financed by the European Union - NextGenerationEU (National Sustainable Mobility Center CN00000023, Italian Ministry of University and Research Decree n. 1033–17/06/2022, Spoke 11 - Innovative Materials & Lightweighting). The opinions expressed are those of the authors only and should not be considered as representative of the European Union or the European Commission's official position. Neither the European Union nor the European Commission can be held responsible for them.

#### References

- [1] Clark, R. (2004). Rail flaw detection: overview and needs for future developments. *Ndt & E International*, 37(2), 111-118.
- [2] Falamarzi, A., Moridpour, S., & Nazem, M. (2019). A review on existing sensors and devices for inspecting railway infrastructure. *Jurnal Kejuruteraan*, 31(1), 1-10.
- [3] Ph Papealias, M., Roberts, C., & Davis, C. L. (2008). A review on non-destructive evaluation of rails: state-of-the-art and future development. *Proceedings of the Institution of Mechanical Engineers, Part F: Journal of Rail and rapid transit*, 222(4), 367-384.
- [4] Netzelmann, U., Walle, G., Lugin, S., Ehlen, A., Bessert, S., & Valeske, B. (2016). Induction thermography: principle, applications and first steps towards standardisation. *Quantitative InfraRed Thermography Journal*, 13(2).
- [5] Tuschl, C., Oswald-Tranta, B., & Eck, S. (2022). Scanning inductive thermographic surface defect inspection of long flat or curved work-pieces using rectification targets. *Applied Sciences*, 12(12), 5851.
- [6] Oswald-Tranta, B., Hackl, A., Lopez de Uralde Olavera, P., Gorostegui-Colinas, E., & Rosell, A. (2022). Calculating probability of detection of short surface cracks using inductive thermography. *Quantitative InfraRed Thermography Journal*, 1-20.
- [7] De Vanna, D., D'Accardi, E., Dell'Avvocato, G., Palumbo, D., & Galietti, U. (2023, June). Induction Thermography: Influence of Testing Parameters for Different Crack Geometry. In *Society for Experimental Mechanics Annual Conference and Exposition* (pp. 73-82). Cham: Springer Nature Switzerland.
- [8] Netzelmann, U., Walle, G., Ehlen, A., Lugin, S., Finckbohner, M., & Bessert, S. (2016, February). NDT of railway components using induction thermography. In *AIP conference proceedings* (Vol. 1706, No. 1). AIP Publishing.
- [9] Zhang, X., Peng, J., Zhang, Q., Tian, K., Tang, S., Liang, X., ... & Gao, X. (2022). Nondestructive analysis of rolling contact fatigue cracks using induced scanning thermography. *Optics Express*, 30(24), 42982-42994.
- [10] D'Accardi, E., Dell'Avvocato, G., Masciopinto, G., Marinelli, G., Fumarola, G., Palumbo, D., & Galietti, U. (2024). Evaluation of typical rail defects by induction thermography: experimental results and procedure for data analysis during high-speed laboratory testing. *Quantitative InfraRed Thermography Journal*, 1-22.

- [11] Tuschl, C., Oswald-Tranta, B., & Eck, S. (2021). Inductive thermography as non-destructive testing for railway rails. *Applied Sciences*, 11(3), 1003.
- [12] ASTM International. *Standard Practice for Probability of Detection Analysis for a Versus a Data*. Designation: E2862, Year, ASTM International. URL.
- [13] Duan, Y., Servais, P., Genest, M., Ibarra-Castanedo, C., Maldague, X.P.: ThermoPoD: A reliability study on active infrared thermography for the inspection of composite materials. *J. Mech. Sci. Technol.* 26(7), 1985–1991 (2012).
- [14] Rothbart, N., Maierhofer, C., Goldammer, M., Hohlstein, F., Koch, J., Kryukov, I., Sengebusch, M.: Probability of detection analysis of round robin test results performed by flash thermography. *Quant. InfraRed Thermogr. J.* 14(1), 1–23 (2017).
- [15] D'Accardi, E., Palumbo, D., Errico, V., Fusco, A., Angelastro, A., & Galietti, U. (2023). Analysing the probability of detection of shallow spherical defects by means of Pulsed Thermography. *Journal of Nondestructive Evaluation*, 42(1), 27.
- [16] Addante, G. D., Dell'Avvocato, G., Bisceglia, F., D'Accardi, E., Palumbo, D., & Galietti, U. (2023). Laser Thermography: An Investigation of Test Parameters on Detection and Quantitative Assessment in a Finite Crack. *Engineering Proceedings*, 51(1), 7.
- [17] Oswald-Tranta, B., de Uralde Olavera, P. L., Gorostegui-Colinas, E., & Westphal, P. (2023, June). Convolutional neural network for automated surface crack detection in inductive thermography. In *Thermosense: Thermal Infra-red Applications XLV* (Vol. 12536, pp. 131-140). SPIE.
- [18] Li, H., Gao, B., Miao, L., Liu, D., Ma, Q., Tian, G., & Woo, W. L. (2020). Multiphysics structured eddy current and thermography defects diagnostics system in moving mode. *IEEE Transactions on Industrial Informatics*, 17(4), 2566-2578.
- [19] Gao, Y., Tian, G. Y., Wang, P., Wang, H., Gao, B., Woo, W. L., & Li, K. (2017). Electromagnetic pulsed thermography for natural cracks inspection. *Scientific reports*, 7(1), 42073.
- [20] DIN 1319-1, Grundlagen der Messtechnik — Teil 1: Grundbegriffe.
- [21] DIN EN 10025-2, Warmgewalzte Erzeugnisse aus Baustähle — Teil 2: Technische Lieferbedingungen für unlegierte Baustähle.
- [22] DIN EN 10088-3, Nichtrostende Stähle — Teil 3: Technische Lieferbedingungen für Halbzeug, Stäbe, Walzdraht, gezogenen Draht, Profile und Blankstahlerzeugnisse aus korrosionsbeständigen Stählen für allgemeine Verwendung.
- [23] DIN 54183, Zerstörungsfreie Prüfung - Thermografische Prüfung - Induktiv angeregte Thermografie. Non-destructive testing - Thermographic testing - Eddy-current excited thermography. Essais non destructifs - Analyses thermographiques - Thermographie excitée par induction.
- [24] Vrana, J. (2008). Grundlagen und Anwendungen der aktiven Thermographie mit elektromagnetischer Anregung: Induktions- und Konduktionsthermographie.
- [25] Jäckel, P., & Netzelmann, U. (2013). The influence of external magnetic fields on crack contrast in magnetic steel detected by induction thermography. *Quantitative InfraRed Thermography Journal*, 10(2), 237-247.
- [26] Oswald-Tranta, B. (2015, October). Untersuchungen zur Bestimmung der Risstiefe mit induktiver Thermografie. In *Thermographie-Kolloquium, Stuttgart*.